Euler–Euler anisotropic Gaussian mesoscale simulation of homogeneous cluster-induced gas–particle turbulence

Bo Kong[1*], Heng Feng[2], Jesse Capecelatro[3], Ravi Patel[4], Olivier Desjardins[4], Rodney O. Fox[1,5]

[1,*]Ames Laboratory – US DOE, Ames, IA 50011-1015, USA

[2]Department of Thermal Engineering,

Tsinghua University, Beijing, PRC

[3]Department of Mechanical Engineering,

University of Michigan, Ann Arbor, MI, USA

[4]Department of Mechanical and Aerospace Engineering,

Cornell University, 305 Upson Hall, Ithaca, NY, USA

[5]Department of Chemical and Biological Engineering,

Iowa State University, Ames, IA 50011-2230, USA

February 14, 2017

1

Abstract

An Euler–Euler anisotropic Gaussian approach (EE-AG) for simulating gas–particle flows, in which particle velocities are assumed to follow a multivariate anisotropic Gaussian distribution, is used to perform mesoscale simulations of homogeneous cluster-induced turbulence (CIT). A three-dimensional Gauss–Hermite quadrature formulation is used to calculate the kinetic flux for ten velocity moments in a finite-volume framework. The particle-phase volume-fraction and momentum equations are coupled with the Eulerian solver for the gas phase. This approach is implemented in an open-source CFD package, OpenFOAM, and detailed simulation results are compared with previous Euler–Lagrange simulations in a domain size study of CIT. The results demonstrate that the proposed EE-AG methodology is able to produce comparable results to EL simulations, and this moment-based methodology can be used to perform accurate mesoscale simulations of dilute gas–particle flows.

Introduction

Gas–particle flows, such as in fluidized beds [1,2,3,4,5,6,7,8,9,10] and risers [11,12,13,14,15,16,17,18,19,20], are widely used in a variety of chemical and energy processes. The accurate simulation of such flows is beneficial for the design and optimization of their industrial applications. Although gas–particle flows in industrial applications are often turbulent, available multiphase turbulence models in commercial computational fluid dynamics codes often lack a rigorous conceptual foundation. In our previous work [21], the exact Reynolds-averaged (RA) equations were derived for the particle phase in a collisional gas–particle flow. To provide closure for various terms in this model and aid its development, mesoscale simulations of homogeneous cluster-induced turbulence (CIT) [22,23,24,25] and wall-bounded vertical channel flow [12,13] have been carried out. CIT refers to the gas-phase turbulence, which is generated and sustained by fluctuations of particle concentration in statistically stationary flows in the absence of mean shear and wall boundaries [25]. The particle concentration fluctuations result from spontaneous particle clustering [11], which is in turn caused by the intimate momentum coupling with the gas-phase, i.e., drag, and gravity. Studying this flow in detail can help us to better understand the key mechanisms in gas–

2

particle turbulence without the interference of turbulence generated by mean shear. Therefore, our early simulation effort has been focused on these types of flows in triply periodic domains to obtain accurate and reliable turbulent statistics. These simulations were performed using an Euler–Lagrange (EL) strategy, in which the particle phase is represented in a Lagrangian manner by tracking finite-size particles individually[26,25].

However, because the multiphase turbulence model we aim to develop itself is based on an Eulerian framework, sophisticated filtering techniques have to be used to extract particle-phase information from EL simulations, e.g., particle granular temperature Θ_p, and the results can be sensitive to various aspects of the filtering process[23,25,12]. By comparison, Euler–Euler (EE) approaches for gas–particle flows can directly provide particle-phase turbulence statistics, and are also well suited for high performance computations, e.g., much less computationally intensive and without problems such as computational "load imbalance" frequently encountered in parallel EL simulations. The two-fluid model (TFM), in which particles are treated in analogy to a fluid in an Eulerian framework, is the most studied and most widely used method when simulating gas–particle flows. Recently, many highly resolved TFM simulations have been conducted for various purposes[9,27,28,29]. The underlining assumption of TFM is that particle velocity distribution is close to Maxwellian, i.e., isotropic, which is valid when particles are densely packed and highly collisional (i.e., Knudsen number < 0.1), such as in dense fluidized beds. With this assumption, the particle phase can be treated with a hydrodynamic model[30,31], and only the five lower-order moments of the velocity distribution function are used to describe the flow, including one zero-order (volume fraction) moment, three first-order (mean velocity) moments, and one second-order velocity moment (granular energy). However, this hydrodynamic description of particle phase has been shown to be inaccurate[32], especially for dilute and very dilute flows, when particle–particle collisions are weak or even negligible. In those situations, the TFM approach cannot capture many key physical phenomena, such as high anisotropy and particle trajectory (or characteristic) crossings (PTC)[33,34,35]. Since turbulence development is often limited when particles are densely packed, here we are mainly interested in dilute gas–particle

3

flows. For such flows, we wish to determine what level of closure is needed to conduct mesoscale simulations to produce physically realistic data as compared to EL simulations.

An alternative EE approach to TFM is quadrature-based moment methods (QBMM), which have been continuously demonstrated to be very successful in overcoming the difficulties of TFM, such as PTC[36,35,15,37,38,39,40]. In general, QBMM find approximate numerical solutions to the kinetic equation of particle velocity distribution by solving the transport equations of different velocity moments sets. Those velocity moments are used to generate quadrature nodes with different reconstruction methods, which in turn can provide closures for various terms in the moment transport equations. In this work, we chose to use the anisotropic Gaussian (AG) closure for gas–particle flows proposed by Vié *et al.*[41], in which the particle velocity is assumed to follow an anisotropic Gaussian distribution. This closure was originally introduced to simulate out-of-equilibrium rarefied gases[42]. In addition to zero- and first-order moments, all six second-order moments are controlled in the AG closure. We hypothesize that it may be a good compromise between physical accuracy and computational stability and cost. The other available approximation methods need more moments to perform simulations in 3-D and the inversion algorithms are more complex. For example, the method developed by Passalacqua *et al.*[37,38] requires at least 20 moments; conditional quadrature method of moments (CQMOM) needs 36 moments for all three permutations[40]. Although the AG model cannot capture the PTC in terms of the number density spatial distribution, it can produce at least the right scale and energetic behavior of PTC[41]. Furthermore, due to the simplicity of this model, the moment-inversion algorithm is the most robust and fast among all published QBMM, and thus well suited for large-scale simulations. In the work of Vié *et al.*[41], only 2-D flows with available analytic solutions were simulated, without considering collisions and coupling with a carrier fluid, in order to accurately evaluate the performance of the AG closure. In this work, an EE solver based on the AG closure (EE-AG) with particle collisions and full coupling between gas and particle phases is developed and implemented in an open-source CFD package, OpenFOAM, which can be used to perform simulations of large-scale and complex gas–particle flows under

4

dilute conditions.

In summary, the primary motivation for this work is to evaluate the ability of the EE-AG solver to capture the main physics of CIT quantitatively by comparing it with EL simulations, and to determine whether it is suitable for conducting mesoscale simulations of dilute gas–particle flows. The EL data chosen to compare with the results of the EE-AG solver were obtained from the EL simulation in a recent study of CIT[24]. The aim of the original EL simulations was to find a large enough computational domain for CIT flow to fully developed[24]. By performing simulations on different domain sizes, the EL simulations provide us unusually detailed data for comparison with EE-AG results. The remainder of this paper is organized as follows. First, we introduce the governing equations of gas–particle flows. Next, we describe the EE-AG solver. Detailed comparisons of the simulation results of the EE-AG and EL methods are then provided, and finally conclusions are drawn.

Governing equations

In this section, the Eulerian governing equations of the gas and particle phases are briefly presented.

Gas phase

The behavior of the gas phase can be described by the mass and momentum transport equations solved in multi-fluid models[43,3].

Continuity

The gas-phase continuity equation derived from a mass balance is

$$\frac{\partial \rho_g \alpha_g}{\partial t} + \nabla \cdot \rho_g \alpha_g \boldsymbol{U}_g = 0 \tag{1}$$

5

where α_g is the gas-phase volume fraction, $\boldsymbol{U}_g$ is the fluid-phase velocity. Here, the gas-phase density ρ_g is assumed to be constant.

Momentum

The gas-phase velocity is found from a momentum balance:

$$\frac{\partial \rho_g \alpha_g \boldsymbol{U}_g}{\partial t} + \nabla \cdot \rho_g \alpha_g \boldsymbol{U}_g \otimes \boldsymbol{U}_g = \nabla \cdot \rho_g \alpha_g \boldsymbol{\sigma}_g - \nabla p_g + \rho_g \alpha_g \boldsymbol{g} - \frac{\rho_p \alpha_p}{\tau_p} \left(\boldsymbol{U}_g - \boldsymbol{U}_p \right) \tag{2}$$

where $\boldsymbol{g}$ is the gravity vector, α_p, ρ_p, $\boldsymbol{U}_p$ are the particle-phase volume fraction, density and velocity, respectively. The gas-phase stress tensor is modeled using a gradient-viscosity model, $\boldsymbol{\sigma}_g = \left(\nu_g + \nu_g^* \right) \left[\nabla \boldsymbol{U}_g + \left(\nabla \boldsymbol{U}_g \right)^T - \frac{2}{3} \left(\nabla \cdot \boldsymbol{U}_g \right) \mathbf{I} \right]$, where ν_g is gas-phase kinematic viscosity, the effective gas viscosity[44] $\nu_g^* = \nu_g \left(\alpha_g^{-2.8} - 1 \right)$. When $\rho_g / \rho_p \ll 1$, as considered in this work, the contribution due to the gas-phase normal stresses (i.e., buoyancy) is negligible[25]. If a constant Stokes drag is used, the drag relaxation time can be calculated as $\tau_p = \rho_p d_p^2 / (18 \rho_g \nu_g)$, where d_p is the particle diameter.

Particle phase

Kinetic equation

Assuming the particles are monodisperse, non-cohesive, constant-density spheres, the particle phase is governed by a kinetic equation for the velocity distribution function $f(\boldsymbol{v})$[33,36,45,30,46,47,31]:

$$\frac{\partial f\left(\boldsymbol{v}\right)}{\partial t} + \mathbf{v} \cdot \frac{\partial f\left(\boldsymbol{v}\right)}{\partial \boldsymbol{x}} + \frac{\partial}{\partial \boldsymbol{v}} \cdot f\left(\boldsymbol{v}\right) \mathbb{A} = \mathbb{C} \tag{3}$$

where $\mathbb{C}$ represents the rate of change in the number density function due to particle collisions, and $\mathbb{A}$ is the particle acceleration due to gravity and drag from the gas phase. As we are interested in dilute gas–particle flows, particle friction is not considered.

6

Moment transport equation

Here, velocity moments are denoted by M_{ijk}^{γ} where $\gamma = i + j + k$ is the order and the subscripts denote the velocity components[46]:

$$M_{ijk}^{\gamma} = \int v_1^i v_2^j v_3^j f(\boldsymbol{v}) \, d\boldsymbol{v}. \tag{4}$$

In this work, we will consider 3-D moments up to second order, and thus the moment vector is

$$\mathbf{M} = \{M_{000}^0, M_{100}^1, M_{010}^1, M_{001}^1, M_{200}^2, M_{110}^2, M_{101}^2, M_{020}^2, M_{011}^2, M_{002}^2\}; \tag{5}$$

and contains the ten independent moments. For convenience, these moments can be re-expressed in terms of a scalar $M_{000}^0 = \rho_p \alpha_p$, a vector

$$\boldsymbol{M}^1 = \begin{bmatrix} M_{100}^1 \\ M_{010}^1 \\ M_{001}^1 \end{bmatrix} = \rho_p \alpha_p \boldsymbol{U}_p, \tag{6}$$

and a symmetric second-order tensor:

$$\mathbf{M}^2 = \begin{bmatrix} M_{200}^2 & M_{110}^2 & M_{101}^2 \\ M_{110}^2 & M_{020}^2 & M_{011}^2 \\ M_{101}^2 & M_{011}^2 & M_{002}^2 \end{bmatrix} = \rho_p \alpha_p \left(\boldsymbol{U}_p \otimes \boldsymbol{U}_p + \mathbf{P}_p \right) \tag{7}$$

where, $\mathbf{P}_p$ is the (non-negative) particle-phase pressure tensor, and the granular temperature $\Theta_p = \frac{1}{3} tr(\mathbf{P}_p)$. Note that knowledge of the moment vector $\mathbf{M}$ is equivalent to knowledge of the ten particle-phase variables $(\alpha_p, \boldsymbol{U}_p, \mathbf{P}_p)$. However, the ten moments are the conserved quantities in the context of a finite-volume approximation.

By integrating Eq. 3 over velocity phase space, a set of transport equations for $\mathbf{M}$ can be

7

obtained:

$$\frac{\partial \mathbf{M}}{\partial t} + \nabla \cdot (\mathbf{F} + \mathbf{G}) = \mathbf{A} + \mathbf{C} \tag{8}$$

where the kinetic spatial fluxes $\mathbf{F}$ are defined in terms of the integer moments of the next higher order[36], and $\mathbf{A}$ is the source term due to drag and gravity. The contribution of particle collisions is divided into a spatial flux $\mathbf{G}$ and a source term $\mathbf{C}$. Now we examine the transport equation of the zero-, first- and second-order moments separately.

The zero-order velocity moment is governed by

$$\frac{\partial M_{000}^0}{\partial t} + \nabla \cdot \boldsymbol{F}_{000}^0 = 0 \tag{9}$$

or, in term of $\rho_p \alpha_p$,

$$\frac{\partial \rho_p \alpha_p}{\partial t} + \boldsymbol{\nabla} \cdot \rho_p \alpha_p \boldsymbol{U}_p = 0. \tag{10}$$

The first-order velocity moments are governed by[46]

$$\frac{\partial \boldsymbol{M}^1}{\partial t} + \nabla \cdot \left(\mathbf{F}^1 + \mathbf{G}^1\right) = \boldsymbol{A}^1 \tag{11}$$

or, in term of $\rho_p \alpha_p \boldsymbol{U}_p$,

$$\frac{\partial \rho_p \alpha_p \boldsymbol{U}_p}{\partial t} + \boldsymbol{\nabla} \cdot \rho_p \alpha_p (\boldsymbol{U}_p \otimes \boldsymbol{U}_p + \mathbf{P}_p + \mathbf{G}_p) = \rho_p \alpha_p \boldsymbol{g} + \frac{\rho_p \alpha_p}{\tau_p} \left(\boldsymbol{U}_g - \boldsymbol{U}_p\right) \tag{12}$$

Here the kinetic flux is $\mathbf{F}^1 = \boldsymbol{U}_p \otimes \boldsymbol{U}_p + \mathbf{P}_p$. The acceleration source term $\boldsymbol{A}^1$ only includes gravity and drag, similar to the gas-phase momentum equation (2). Since particle–particle collisions do not changed the particle-phase mean momentum, the collisional source term is null. Using the Enskog–Boltzmann kinetic theory, the collisional flux tensor $\mathbf{G}_p$ can be written as[46]

$$\mathbf{G}_p = \frac{4}{5}\eta \alpha_p g_0 \left(3\Theta_p \mathbf{I} + 2\mathbf{P}_p\right) \tag{13}$$

where $\eta = \frac{1}{2}(1 + e)$, e is the particle collision restitution coefficient, and the particle radial

8

distribution function g_0 can be modeled as, $g_0 = \left(1 - \frac{1}{2}\alpha_p\right)/(1 - \alpha_p)^3$ [48,49].

The second-order velocity moments are governed by [46]

$$\frac{\partial \mathbf{M}^2}{\partial t} + \nabla \cdot \left(\mathbf{F}^2 + \mathbf{G}^2\right) = \mathbf{A}^2 + \mathbf{C}^2 \tag{14}$$

or, in term of $\rho_p \alpha_p \left(\boldsymbol{U}_p \otimes \boldsymbol{U}_p + \mathbf{P}_p\right)$,

$$\frac{\partial}{\partial t} \rho_p \alpha_p (\boldsymbol{U}_p \otimes \boldsymbol{U}_p + \mathbf{P}_p)$$
$$+ \boldsymbol{\nabla} \cdot \rho_p \alpha_p (\boldsymbol{U}_p \otimes \boldsymbol{U}_p \otimes \boldsymbol{U}_p + \mathbf{P}_p \otimes \boldsymbol{U}_p + \boldsymbol{U}_p \otimes \mathbf{P}_p + [\![P_{p,ik}U_{p,j}]\!] + \mathbf{Q}_p + \mathbf{H}_p) =$$
$$\rho_p \alpha_p (\boldsymbol{U}_p \otimes \boldsymbol{g} + \boldsymbol{g} \otimes \boldsymbol{U}_p) + \rho_p \alpha_p \boldsymbol{E}_{fp} + \rho_p \alpha_p \boldsymbol{C}_p \tag{15}$$

where we have introduced the kinetic-flux tensor $\mathbf{Q}_p$, due to third-order central moments, and the collisional-flux tensor $\mathbf{H}_p$, the symmetric, second-order, energy-coupling-with-the-fluid-phase tensor $\boldsymbol{E}_{fp}$, and the collision source term tensor $\boldsymbol{C}_p$. In (15), $[\![P_{p,ik}U_{p,j}]\!]$ is a third-order tensor with components $P_{p,ik}U_{p,j}$. By manipulating the transport equations, (15) can be replaced by a transport equation for $\mathbf{P}_p$ [25]:

$$\frac{\partial \rho_p \alpha_p \mathbf{P}_p}{\partial t} + \boldsymbol{\nabla} \cdot \rho_p \alpha_p (\boldsymbol{U}_p \otimes \mathbf{P}_p + \mathbf{Q}_p + \mathbf{H}_p) =$$
$$- \rho_p \alpha_p \left[\mathbf{P}_p \cdot \boldsymbol{\nabla}\boldsymbol{U}_p + (\mathbf{P}_p \cdot \boldsymbol{\nabla}\boldsymbol{U}_p)^T\right] - \rho_p \alpha_p \frac{2}{\tau_p} \mathbf{P}_p + \rho_p \alpha_p \frac{2}{\tau_c} (\Delta^* - \mathbf{P}_p). \tag{16}$$

Here the collisional source term for $\mathbf{P}_p$ is described using a linearized Bhatnagar–Gross–Krook (BGK) inelastic collision model [50], with the collisional time $\tau_c = d_p/\left(6\alpha_p g_0 \sqrt{\Theta_p/\pi}\right)$, and $\Delta^* = \eta^2 \Theta_p \mathbf{I} + (1 - \eta)^2 \mathbf{P}_p$. The spatial fluxes can be closed with a gradient-diffusion model: $\mathbf{Q}_p + \mathbf{H}_p = -k_p \boldsymbol{\nabla} \otimes \mathbf{P}_p$, where k_p is the granular conductivity, which can be related to ν_p. Note that first term on the right-hand side of (16) is a source term that arises due to the non-conservative form of the kinetic energy balance. When higher-order velocity moments are used to define the velocity distribution function, the conservative form in (15) is preferable.

9

EE-AG solver

In this work, the particle velocity distribution $f(\boldsymbol{v})$ is approximated using the AG distribution[41]:

$$f(\boldsymbol{v}) = \frac{\alpha_p}{(2\pi|\mathbf{P}_p|)^{3/2}} \exp\left[-\frac{1}{2}(\boldsymbol{v} - \boldsymbol{U}_p) \cdot \mathbf{P}_p^{-1} \cdot (\boldsymbol{v} - \boldsymbol{U}_p)\right]. \tag{17}$$

It is apparent that this distribution can be determined by three variables: α_p, $\boldsymbol{U}_p$, $\mathbf{P}_p$, which can directly be found from the moment set $\mathbf{M}$. Without higher-order moments, the AG closure is unable to capture particle trajectory crossing accurately. However, in many industrial applications, extremely dilute gas–particle flows are rare. The aim of this work is to demonstrate that the EE model with AG closure can produce comparable results with EL simulations. With this assumption, we solve the moment transport equation (8) using a weakly coupled operator-splitting method, i.e., treating the terms $\mathbf{F}$, $\mathbf{A}$, $\mathbf{C}$ and $\mathbf{G}$ in (8) separately as described next.

Kinetic moment flux

The most important point in solving the moment transport equation is to provide a closure for the moment spatial flux $\mathbf{F}$, which is treated using a kinetic-based finite-volume (KBFV) scheme with a 3-D Gauss–Hermite quadrature approximation for the AG distribution. First, the AG distribution can be approximated using quadrature as follows:

$$f(\boldsymbol{v}) := \alpha_p \sum_{\alpha=1}^{N_{hq}^3} \tilde{\rho}_\alpha \delta(\boldsymbol{v}, \tilde{\boldsymbol{v}}_\alpha) = \alpha_p \sum_{i=1}^{N_{hq}} \sum_{j=1}^{N_{hq}} \sum_{k=1}^{N_{hq}} \rho_i \rho_j \rho_k \delta\left(\boldsymbol{v}, \mathbf{R} \cdot \begin{bmatrix} u_i \\ v_j \\ w_k \end{bmatrix} + \boldsymbol{U}_p\right) \tag{18}$$

where ρ_i, ρ_j, ρ_k and u_i, v_j, w_k are the weights and abscissas of the Gauss–Hermite quadrature of the standard normal distribution with zero mean and unit variance:

$$N(x|0, 1) = \frac{1}{\sqrt{2\pi}} \exp\left(-\frac{x^2}{2}\right) \models \sum_{i=1}^{N_{hq}} \rho_i \delta(x, u_i) \tag{19}$$

10

where $\models$ is understood to mean that the moments M_i for $i \in \{0, 1, \ldots, 2N_{hq} - 1\}$ of the two distribution functions are equal. The rotation tensor is $\mathbf{R} = \mathbf{Q} \cdot \sqrt{\mathbf{\Lambda}}$, and $\mathbf{Q} \cdot \mathbf{\Lambda} \cdot \mathbf{Q}^T = \mathbf{P}_p$ is the spectral decomposition of particle granular pressure tensor $\mathbf{P}_p$, where a highly efficient spectral decomposition algorithm for $3{\times}3$ matrix[51] is used. Note that since the quadrature weights $\tilde{\rho}_\alpha$ and the quadrature vector $[u_i, v_j, w_k]^T$ are independent of $\alpha_p, \boldsymbol{U}_p$ and $\mathbf{P}_p$, they can be computed and stored at the beginning of a simulation. A simple 2-D example is given in Fig. 1 to illustrate the quadrature approximation of the AG distribution.

[Figure 1 about here.]

In a finite-volume framework, the kinetic-based moment spatial fluxes on cell faces are decomposed into two contributions as follows[33,34,38]:

$$
\begin{aligned}
F_{i,j,k}^x &= \int_0^\infty u^{i+1} v^j w^k f(\boldsymbol{v}) \, d\boldsymbol{v} + \int_{-\infty}^0 u^{i+1} v^j w^k f(\boldsymbol{v}) \, d\boldsymbol{v} \\
&= \sum_{\alpha=1}^{N_{hq}^3} \max(\tilde{u}_\alpha, 0) \tilde{\rho}_\alpha \tilde{u}_\alpha^i \tilde{v}_\alpha^j \tilde{w}_\alpha^k + \sum_{\alpha=1}^{N_{hq}^3} \min(\tilde{u}_\alpha, 0) \tilde{\rho}_\alpha \tilde{u}_\alpha^i \tilde{v}_\alpha^j \tilde{w}_\alpha^k
\end{aligned}
\tag{20}
$$

where $\tilde{u}_\alpha, \tilde{v}_\alpha, \tilde{w}_\alpha$ are the x, y, z component of velocity abscissas $\boldsymbol{v}_\alpha$. The kinetic-based fluxes in the y and z directions are calculated in a similar matter. Since the reconstruction of velocity distribution of Eq. (18) is performed at cell centers once, the flux calculation at cell faces in Eq. (20) is carried out at all cell faces of that cell, which determines the accuracy of this calculation to be first order, which is the same as the schemes used in[35,37,38,40]. However, the extension to higher-order spatial fluxes can be done as described by Vikas *et al.*[52,53,41]. Notice that with the AG closure, the kinetic flux term $\mathbf{Q}_p$ for the second-order velocity moments is null, since the third-order central moments for a multivariate Gaussian distribution are zero.

11

To guarantee that the resulting moments are realizable, the time step has to be fixed by setting an overall time-step condition:

$$\Delta t = \min_{\Omega} \left[\text{CFL} \min_{\alpha} \left(\frac{\Delta x}{|\tilde{u}_\alpha|}, \frac{\Delta y}{|\tilde{v}_\alpha|}, \frac{\Delta z}{|\tilde{w}_\alpha|} \right), \text{CFL} \min \left(\frac{\Delta x}{|\boldsymbol{U}_{g,x}|}, \frac{\Delta y}{|\boldsymbol{U}_{g,y}|}, \frac{\Delta z}{|\boldsymbol{U}_{g,z}|} \right), \frac{1}{10} \min(\tau_p, \tau_c) \right]$$

(21)

where Ω indicates the whole computation domain and $0 < \text{CFL} \leq 1$ is the CFL number. For the dilute flows considered in this work, the overall time step was determined from the CFL time step, which was found to be small relative to τ_p and τ_c. Note that for denser flows where τ_c is much smaller than the other time scales, the particle-phase equations reduce to the classical hydrodynamic model[30,31]. For such cases, an iterative, implicit algorithm that does not depend explicitly on τ_c should be employed (see[54] for details).

Collisional flux and source term

The effect of particle–particle collisions appears as the collisional momentum flux $\mathbf{G}_p$ in Eq. (12) and the collisional heat flux for second-order velocity moments $\mathbf{H}_p$ and the collision dissipation source term $\boldsymbol{C}_p$ in Eq. (14). In the dilute limit, $\mathbf{H}_p$ is negligible, so we only consider $\mathbf{G}_p$ and $\boldsymbol{C}_p$ by solving the following equations:

$$\frac{\partial \boldsymbol{U}_p}{\partial t} = -\nabla \cdot \mathbf{G}_p$$

(22)

and

$$\frac{\partial \mathbf{P}_p}{\partial t} = \frac{2}{\tau_c} \left(\Delta^* - \mathbf{P}_p \right).$$

(23)

Note that the spatial divergence of $\mathbf{G}_p$ appears in Eq. (22), which can be computed explicitly and directly used to solve the change of $\boldsymbol{U}_p$ in dilute gas–particle flows. The characteristic time scales for (22) and (23) are proportional to τ_c, which is used in the time-step condition in (21).

12

Drag and gravity

Previously, when QBMM were used to treat the velocity distribution, the effect of drag and gravity on particle velocity was usually calculated on individual velocity abscissas [55,32] by solving an ordinary differential equation (ODE):

$$\frac{d\tilde{\boldsymbol{v}}_\alpha}{dt} = \frac{1}{\tau_p}\left(\boldsymbol{U}_g - \tilde{\boldsymbol{v}}_\alpha\right) + \boldsymbol{g}. \tag{24}$$

In general, τ_p also has to be calculated individually for each velocity abscissas as a function of $Re_p = \alpha_g d_p |\boldsymbol{U}_g - \tilde{\boldsymbol{v}}_\alpha| / \nu_g$. However, a linearized drag model can be applied without losing much accuracy. Furthermore, in the CIT simulations a constant Stoke drag is used, which is independent of particle velocity. Thus, the acceleration source term $\mathbf{A}$ is directly accounted for by solving the following ODEs for $\boldsymbol{U}_p$ and $\mathbf{P}_p$:

$$\frac{\partial \boldsymbol{U}_p}{\partial t} = \frac{1}{\tau_p}\left(\boldsymbol{U}_g - \boldsymbol{U}_p\right) + \boldsymbol{g} \tag{25}$$

and

$$\frac{\partial \mathbf{P}_p}{\partial t} = -\frac{2}{\tau_p}\mathbf{P}_p. \tag{26}$$

In the simulation code, operator splitting is used for time advancement, and the drag and gravity contributions are treated separately after the spatial fluxes and collisions in order to ensure realizability of the moments. With this, all the terms appearing in the three transport equations (9), (11), and (14) are accounted for.

Gas-phase solver

Once the particle phase is solved, the continuous gas phase is solved in a similar manner as in our previous works [55,32,56]. The semi-discretized momentum equation for the gas phase (2) is

$$\mathbb{A}_g \boldsymbol{U}_g = \mathbb{H}_g + \rho_g \alpha_g \boldsymbol{g} - K_{gp}\left(\boldsymbol{U}_g - \boldsymbol{U}_p\right) - \nabla p_g \tag{27}$$

13

where $\mathbb{H}_g$ includes the off-diagonal contributions, $\mathbb{A}_g$ contains the diagonal coefficients, and $K_{gp} = \rho_p \alpha_p / \tau_p$ is the drag coefficient. By defining $\lambda_g = (\mathbb{A}_g + K_{gp})^{-1}$, the gas-phase velocity can expressed as

$$\boldsymbol{U}_g = \lambda_g \left(\mathbb{H}_g + \rho_p \alpha_g \boldsymbol{g} + K_{gp} \boldsymbol{U}_p - \nabla p_g \right). \tag{28}$$

The face velocity flux for the gas phase can be computed as

$$\boldsymbol{\phi}_g = (\lambda_g \mathbb{H}_g)_f \cdot \boldsymbol{S} + \lambda_{g,f} \rho_g \alpha_{g,f} \boldsymbol{g} \cdot \boldsymbol{S} + \lambda_{g,f} (K_{gp} \boldsymbol{U}_p)_f \cdot \boldsymbol{S} - \lambda_{g,f} |\boldsymbol{S}| \nabla^{\perp} p_g. \tag{29}$$

To solve for the gas pressure, the gas continuity equation (1) and the relation $\alpha_g + \alpha_p = 1$ is used. Substituting $\boldsymbol{\phi}_g$ in place of $\boldsymbol{U}_g$ and rearranging the terms, we obtain the gas-phase pressure equation:

$$(\alpha_g \lambda_g)_f |\boldsymbol{S}| \nabla^{\perp} p_g = -\frac{\partial \alpha_p}{\partial t} + \alpha_{g,f} \left[(\lambda_g \mathbb{H}_g)_f \cdot \boldsymbol{S} + \lambda_{g,f} \rho_g \alpha_{g,f} \boldsymbol{g} \cdot \boldsymbol{S} + \lambda_{g,f} (K_{gp} \boldsymbol{U}_p)_f \cdot \boldsymbol{S} \right] \tag{30}$$

where $\partial \alpha_p / \partial t$ is the rate of particle volume fraction change due to particle free transport, calculated explicitly when solving Eq. (9). Once the new gas-phase pressure field is computed, the gas-phase velocity can be updated with (28). Note that the equations above are discretized in time with an Euler scheme, which is first-order accurate.

Overall solution algorithm for EE-AG simulations

The solution algorithm for the calculations described above is similar to what was applied in[55,32,56], which is briefly introduced as follows:

1. Initialize all variables $\mathbf{M}$, $\{\alpha_p, \boldsymbol{U}_p, \boldsymbol{P}_p\}$, and $\{\alpha_g, \boldsymbol{U}_g, p_g\}$.

2. Determine Δt using time-step condition in (21).

3. Compute kinetic-based moment fluxes in (20) to transport the moments $\mathbf{M}$. Use updated $\mathbf{M}$ to compute updated $\{\alpha_p, \boldsymbol{U}_p, \boldsymbol{P}_p\}$ and α_g.

14

4. Account for particle–particle collisions by solving Eq. (22) and (23).

5. Account for drag and gravity force by solving Eq. (25) and (26).

6. Update moment set $\mathbf{M}$ using new $\{\alpha_p, \boldsymbol{U}_p, \boldsymbol{P}_p\}$.

7. Construct fluid-phase velocity equation (28), and solve gas-phase pressure equation (30), and update gas-phase velocity with the new pressure. Iterate until gas-phase pressure is converged.

8. Advance in time by repeating from Step 2 until simulation is complete.

This algorithm was implemented in the open-source CFD package, OpenFOAM. The gas-phase equations above are solved with OpenFOAM default first-order implicit "Euler" scheme in time and second-order "linear" interpolation scheme in space. The periodic boundary condition used in the simulations below is the standard "cyclic" boundary in OpenFOAM. Note that the applicability of this algorithm is limited to the dilute flow regime (i.e. $\langle \alpha_p \rangle < 0.05$). A more general algorithm for simulating fluid–particle flows across all flow regimes is proposed in[54].

Comparison between EL and EE-AG simulations of CIT

In this section, the simulation conditions are briefly described first. Then the simulation results are presented and discussed in detail.

Simulation conditions

The mesoscale simulations of CIT using the EE-AG solver were carried out using the exact same physical parameters and 3-D computational mesh as in the EL simulations[24], which are briefly described below. The simulated CIT flow can be characterized by two main parameters: mass loading, $\phi = \rho_p \langle \alpha_p \rangle / (\rho_g \langle \alpha_g \rangle) = 10.1$, and particle Reynolds number, $\mathrm{Re}_p = \tau_p \boldsymbol{g} d_p / \nu_g = 0.5$. These values were achieved by using a constant Stokes drag and by setting the physical parameters using the values listed in Table 1. The mean vertical gas velocity was maintained

15

at zero by applying a body force to the gas phase. Note that the particle settling velocity $\mathcal{V} = \tau_p g = 0.1$ m/s is used to normalize the velocity data in the results presented below.

[Table 1 about here.]

Measured by a characteristic cluster length, $\mathcal{L} = \tau_p^2 g = 2.5$ mm, six different computational domain sizes were studied: $L_x/\mathcal{L} = 4, 8, 16, 32, 65$ and 129 where L_x is the vertical length. The different domain sizes are referred to as Cases 1–6, as was done in the EL simulations[24]. The computational domains are triply periodic with $L_x = 4L_y = 4L_z$. The computational mesh is uniform with grid spacing $d_x = d_y = d_z = 1.75d_p$. The largest computational domain (Case 6) was thus $2048 \times 512 \times 512$ grid cells. Each case was run until the flow reached a statistically stationary state before collecting statistical data.

Results and discussion

Before introducing the results of the EL and EE-AG simulations, it is useful to first review some of the key differences between these two approaches, beyond the different frameworks, i.e., EL vs. EE, and AG closure, and their expected impact on the CIT simulation results. First, particle collisions are treated exactly in EL, while they are modeled with an anisotropic BGK closure in EE-AG. The impact of this difference on the main statistics should be limited, due to the fact that granular energy dissipation through inelastic collisions is very small compared to gas-phase viscous dissipation[25]. Second, a filter is used in the EL simulations to couple the Lagrangian particle velocity to the gas-phase velocity, while the coupling with the fluid is exact in the EE-AG solver. Third, the kinetic flux scheme used in the current EE-AG solver is first-order accurate, while Lagrangian particle tracking in the EL approach is much more accurate. This means that the EE-AG simulations will be more diffusive than the EL simulations. Both the differences in coupling and the convection scheme will lead to different behaviors at small scales, as we will see in the following results. Finally, the Eulerian quantities of Lagrangian particles are extracted from the EL simulations with an adaptive filter technique[23,25], while in

16

the EE-AG simulations, all particle variables are defined at the grid-cell level. The consequence of this difference is that the quantities produced by the two simulations could be comparable on large scales, but different on small scales close to the filter size.

Particle clustering

[Figure 2 about here.]

As depicted in Fig. 2, the particle clustering shown in the instantaneous particle fields produced by EL simulations and the particle-phase volume fraction fields generated by EE-AG simulations are similar in both relative size and shape, but with EE-AG exhibiting slightly longer/wider clusters. There is a clear dependence on the domain size. The clusters appear to be vertically elongated, allowing them to fall faster than the terminal velocity of an isolated particle. The clusters are broken up by the wakes of the entrained gas phase[22]. To quantitatively compare the degree of particle segregation, the deviation of volume fraction from a randomly distributed field of particles, $D = (\langle \alpha_p'^2 \rangle^{1/2} - \sigma_p)/\langle \alpha_p \rangle$, where $\sigma_p = 0.0028$ is the standard deviation of a corresponding flow with a random distribution of particles described in Table 1, are plotted against domain size in Fig. 3. Both EE-AG and EL simulations predict that the volume fraction fluctuations grow with domain size, and the agreement between them is remarkably good, with the values produced by the EE-AG solver being only slightly lower than the EL results.

[Figure 3 about here.]

[Figure 4 about here.]

Also notice that there are no particle clusters observed in the EE-AG simulation with the smallest domain. Since the EL approach can be considered arbitrarily high order in space, while the EE-AG solver employed here is only first-order spatially, the slight under-prediction of particle clustering is understandable. To view this difference more clearly, the probably density

17

functions (PDF) of the particle volume fraction were calculated and plotted in Fig. 4 for the two largest domain sizes. Although the overall agreement is good, it is interesting to observe that the EE-AG solver produces less high volume fraction values, i.e., shorter tails of the PDF function, which improves with bigger domain size. Also considering that the overall volume fraction fluctuations given by EE-AG is consistently less than those by EL, we argue this could be an artifact of the numerical scheme because the first-order scheme employed in the EE-AG simulation is more diffusive.

Particle settling velocity

[Figure 5 about here.]

The particle clusters appearing in the simulations described earlier entrain carrier gas around them, which reduces the local drag and lets them fall faster[22,25]. Thus, since the particle segregation is increasing with domain size, the magnitude of mean particle settling velocity will keep increasing[24], as shown in Fig. 5. As described in[21], the settling velocity is determined by the drift velocity, which is also referred to as the fluid velocity seen by the particles. As fluid is entrained by the clusters, the drift velocity is closer to the particle-phase velocity, allowing the particles to fall faster than the terminal velocity. Therefore, the good agreement between EL and EE-AG simulations in particle volume fraction fluctuations in Fig. 3 certainly leads to good agreement in the settling velocity, as we observe in Fig. 5. In the smallest domain, since no particle clusters appeared, the settling velocity becomes the terminal velocity of an isolated particle $\mathcal{V}$. In the largest domain, both simulations predict a mean settling velocity of approximately $2.5\mathcal{V}$, with the values from EE-AG being slightly higher than those from EL. This finding seems to be contrary to the conclusion suggested by particle volume fraction PDF function, i.e., the flow predicted by EE-AG is slightly less heterogeneous compared to EL. However, it is consistent with the observation from the instantaneous volume fraction fields that the EE-AG clusters are longer/larger than those from EL, considering that longer particle clusters will reduce drag and lead to a higher particle settling velocity. We argue that the more

18

elongated particle clusters in EE-AG could be the consequence of different coupling strategy used in EE-AG and EL simulations, namely, being exact in EE-AG and utilizing an isotropic Gaussian filter in EL. This difference in phase-coupling could mean that it is harder for particles to penetrate the gas phase in EL than in EE-AG, as we can see in the two-point spatial correlation data presented below.

One-point phasic fluctuating energy statistics

The particle-phase (uncorrelated) granular energy, $\frac{3}{2}\langle\Theta_p\rangle_p$, (correlated) turbulent kinetic energy[21], $k_p = \frac{1}{2}\langle\boldsymbol{U}_p'' \cdot \boldsymbol{U}_p''\rangle_p$, and the fluid-phase turbulent kinetic energy, $k_g = \frac{1}{2}\langle\boldsymbol{U}_g''' \cdot \boldsymbol{U}_g'''\rangle_g$, are shown in Fig. 6 with their respective anisotropy. $\langle\phi\rangle_f = \langle\alpha_f\phi\rangle / \langle\alpha_f\rangle$ denotes the phase average of quantity ϕ with respect to phase volume fraction α_f. The particle velocity fluctuation of the particle phase and the gas phase are calculated by $\boldsymbol{U}_p'' = \boldsymbol{U}_p - \langle\boldsymbol{U}_p\rangle_p$ and $\boldsymbol{U}_g''' = \boldsymbol{U}_g - \langle\boldsymbol{U}_g\rangle_g$, respectively. Note that the particle-phase total fluctuation energy is $\kappa_p = k_p + \frac{3}{2}\langle\Theta_p\rangle_p$. All variables in Fig. 6 are normalized using their respective particle settling velocity given in Fig. 5.

[Figure 6 about here.]

In general, the fluctuating energy increases with domain size, which is expected since the production term is proportional to the square of the drift velocity[21,25] and the latter increases with domain size (see Fig. 5). Furthermore, most of the energy is contained in the largest scales, which are not resolved on the smaller domains. More importantly, the values predicted by the EE-AG and EL simulations show the same trends with domain size. Because TKE production occurs only in the fluid phase[21], and the drift velocity in the EE-AG simulations are slightly larger than in the EL simulations, the difference in the fluid-phase TKE in Fig. 6e is most likely due to the latter. Although Fig. 6a shows the uncorrelated granular energy predicted by the EE-AG simulations is significantly lower than the values predicted by EL, the overall contribution of granular energy to the total fluctuations, i.e., $\frac{3}{2}\langle\Theta_p\rangle_p / \kappa_p$ is generally low in the simulated cases, less than 10% in both EL and EE-AG simulations. This difference will be further discussed together with other statistics below.

19

Due to the fact that TKE production is only in the vertical direction, the fluctuating energy components in CIT are highly anisotropic[25]. In Fig. 6, the normalized vertical component of the particle-phase fluctuating energy are shown for the EE-AG and EL simulations. Note that by definition, $P_{p,xx} + P_{p,yy} + P_{p,zz} = 3\Theta_p$ and $\langle U_{p,x}^{'',2} \rangle_p + \langle U_{p,y}^{'',2} \rangle_p + \langle U_{p,z}^{'',2} \rangle_p = 2k_p$. The overall high anisotropy shown in the figure indicates that the contribution of vertical (x) components to the respective kinetic energy are much larger than the contributions of horizontal (y and z) components, as expected. When the domain size is small, the limited turbulence development leads to near unity particle velocity anisotropy in both uncorrelated and correlated kinetic energy. As the domain size increases, the anisotropy predicted from both EL and EE-AG simulations approaches a constant value, which is near 0.8 for turbulent kinetic energy, and between approximately 0.5 and 0.6 for the uncorrelated granular energy. In general, the EE-AG simulations predict higher anisotropy than the EL simulations, especially for granular energy. Both this difference and the relatively higher granular energy and lower turbulent kinetic energy predictions shown in Fig. 6a and 6c may be due to how those quantities were computed in these two simulations. Namely, an adaptive filter was used to extract data from the EL simulations, which means that the correlated and uncorrelated particle fluctuation energy in the EL simulations are measured on larger length scales than in the EE-AG simulations. Another possible explanation for this difference is the different momentum coupling methods employed in the EL and EE-AG simulations. Since the coupling filter in the EL simulations acts on a scale defined by, $\delta_f = 10d_p$, on average, the gas phase in the EL simulations can "feel" the presence of the particles from larger distances than in the EE-AG simulations, which will lead to different gas TKE production and spatial distribution, and in turn cause different particle velocity energy orientation. In the following section, the energy spectrum analysis of volume fraction and velocity will demonstrate the effect of the EL filtering more clearly.

20

Two-point spatial statistics

While one-point statistics provide a general picture of CIT statistics, two-point statistics give a more detailed assessment of the spatial structure of the various fluctuating fields. Here, we present one-dimensional energy spectral density for the volume fraction and velocity fields, as well as two-point spatial correlation functions in the vertical and horizontal directions. We choose to present the data from the two largest domain size cases, where CIT can be considered close to fully developed.

The energy spectra, i.e., energy spectral density (ESD), for particle volume fraction, particle velocity and gas velocity are computed with the following equations and shown in Fig. 7:

$$E_{\alpha_p} = \frac{1}{\langle \alpha_p \rangle^2} \left\langle FFT \left(\alpha_p' \right)^2 \right\rangle, \tag{31}$$

$$E_{\boldsymbol{U}_{p,x}} = \frac{1}{\langle \alpha_p \rangle} \left\langle FFT \left(\sqrt{\alpha_p} \boldsymbol{U}_{p,x}'' \right)^2 \right\rangle, \qquad E_{\boldsymbol{U}_{g,x}} = \frac{1}{\langle \alpha_g \rangle} \left\langle FFT \left(\sqrt{\alpha_g} \boldsymbol{U}_{g,x}''' \right)^2 \right\rangle \tag{32}$$

where FFT represents the fast Fourier transform in one spacial direction, and $\langle \cdot \rangle$ denote the spatial averaging in the other two directions. Note that the spectral density calculated here are not to be confused with a power spectrum, i.e., power spectral density (PSD), since they are not averaged with the signal length of the FFT. Considering the good agreement in both deviation of volume fraction fluctuations and TKE for both the gas and particle phases from EL and EE-AG simulations, we expect to see good agreement also in ESD in the low wavenumber region, where the energy is concentrated. Figure 7 also clearly demonstrates that the EL and EE-AG spectra diverge to the wavenumber corresponding to the length scale where the filtering in EL starts to take effect, most visibly in the horizontal direction. Note that highest wavenumber corresponds to the computation grid size, which is $d_{x,y,z} = 1.75 d_p$. It is speculated that some uncorrelated granular energy at high wavenumber was not entirely removed from particle velocities by the adaptive filtering process in the EL simulations. With this, it also can be argued that this leads to the higher energy spectra values at high wavenumber/small length scale in the EL simulation, as

21

a consequence of this filtering, and leads to higher granular energy and lower velocity anisotropy observed in Fig. 6. The other interesting observation is that for the EL simulations, the vertical energy spectra of particle volume fraction almost entirely overlap with the horizontal spectra, while they only partially collapse with each other at the high wavenumber region for particle velocity. This is not the case for the EE-AG simulations: the vertical spectra generally have less energy at high frequencies, and the volume fraction spectra seem to improve with bigger domain size. Like the PDF of particle volume fraction, we argue this could be another artifact of the first-order scheme employed in the EE-AG simulation, which is more diffusive in the main convective (vertical) direction than in the traverse direction, while the convection scheme employed in the EL simulations has no directional preference.

[Figure 7 about here.]

The spatial correlation of particle volume fraction, i.e., radial distribution function (RDF), and spatial correlation of particle velocity can be calculated by the two following equations[23]:

$$g_0\left(r\boldsymbol{e}_i\right) = \frac{\langle \alpha_p\left(x,t\right)\alpha_p\left(x+r\boldsymbol{e}_i,t\right)\rangle}{\langle \alpha_p\left(x,t\right)\rangle\langle \alpha_p\left(x+r\boldsymbol{e}_i,t\right)\rangle}, \tag{33}$$

$$R\left(r\boldsymbol{e}_i\right) = \frac{\left\langle \alpha_p\left(x,t\right)\alpha_p\left(x+r\boldsymbol{e}_i,t\right)\boldsymbol{U}_p^{''}\left(x,t\right)\cdot\boldsymbol{U}_p^{''}\left(x+r\boldsymbol{e}_i,t\right)\right\rangle}{\left\langle \alpha_p\left(x,t\right)\alpha_p\left(x+r\boldsymbol{e}_i,t\right)\right\rangle}. \tag{34}$$

The vertical and horizontal RDF of both EE-AG and EL simulations are given in Fig. 8, and particle velocity correlations are shown in Fig. 9. Both correlation functions of EE-AG in the vertical direction are wider than those from EL simulations (indicating longer structures), but agree well in the horizontal direction. This directional difference could be another artifact of the different numerical schemes in EL and EE-AG, as observed with the energy spectra. But it also could be argued that particle clusters in EE-AG simulations travel longer distances downwards before they are broken up by gas-phase turbulence than in the EL simulations, due to the smaller coupling length scale felt by the surrounding gas. Also notice that the integral length scale of particle volume fractions are similar for both $L_x/\mathcal{L} = 65$ and 129, which demonstrates that

22

the cluster size is independent of domain size in these two largest cases. This is not true for the spatial correlations of particle velocity, which appear to show similar function shapes on a doubled length scale, i.e., "self-similar" on domain size. As discussed for the TKE, we attribute this to the fact that the energy is mostly in the largest resolved scales.

[Figure 8 about here.]

[Figure 9 about here.]

Conclusions

An Euler–Euler gas–particle flow solver based on the anisotropic Gaussian closure for the particle velocity distribution (EE-AG) has been developed and implemented in OpenFOAM. This method solves transport equations for ten velocity moments up to second order. The ability of the EE-AG solver to capture the main physics of dilute, gravity-driven, gas–particle flows was evaluated by performing detailed comparisons of its simulation results with Euler–Lagrangian simulations used in a domain-size study of homogeneous CIT flows.

In general, we have shown that EE-AG can provide statistical results in satisfactory agreement with those produced using an EL strategy, including one-point statistics, such as deviation of volume fraction, particle mean settling velocity and granular energy, and TKE of both the particle and gas phases; and two-points statics, such as energy spectra and spatial correlations. Thus, the main observation in this study is that solving transport equations for the particle-phase volume fraction, velocity and pressure tensor in a Eulerian framework with an anisotropic Gaussian closure produces results comparable to Euler–Lagrangian simulations. The observed differences in the statistical results, such as in the velocity anisotropy and two-point statistics, can be partially attributed to the two different numerical methods employed in EL and EE-AG, i.e., the convection scheme and the coupling to the gas phase, and different post-processing methods, i.e., the adaptive filtering used in the EL simulations.

23

The computational cost of the EE-AG and EL solvers are not directly compared in this work, considering that different programming languages, code structures and linear solver algorithms for the gas-phase pressure equation are used in EL and EE-AG simulations. The computational algorithm for the particle phase is fairly simple and can be highly efficient in parallel, thus the cost of the kinetic-based AG solver itself is low compared with Lagrangian particle tracking. Overall, we conclude that the EE-AG solver developed in this work can be used to study dilute CIT as quantitatively as the EL approach, and the unclosed terms in gas–particle turbulence models can be investigated using either method.

Finally, the objective of future work is to utilize the spectral analysis as a tool to improve the adaptive filtering technique for the EL simulations in order to achieve accurate separation of correlated and uncorrelated particle fluctuation energy. A detailed comparison study of the behaviors of TFM, QBMM and EL approaches is also warranted as a next step. The extension of the EE-AG solver to other flow regimes (e.g. dense fluidized beds) is described in [54].

Acknowledgments

24

Literature Cited

1 Anderson TB, Jackson R. Fluid mechanical description of fluidized beds. Equations of motion. *Industrial & Engineering Chemistry Fundamentals*. 1967;6(4):527–539.

2 Dan S, Jianzhi W, Huilin L, Yunhua Z, Juhui C, Gidaspow D, Ming C. Numerical simulation of gas–particle flow with a second-order moment method in bubbling fluidized beds. *Powder Technology*. 2010;199(3):213–225.

3 Gidaspow D. *Multiphase flow and fluidization: Continuum and kinetic theory descriptions*. New York, USA: Academic Press. 1994.

4 Herzog N, Schreiber M, Egbers C, Krautz HJ. A comparative study of different CFD-codes for numerical simulation of gas–solid fluidized bed hydrodynamics. *Computers & Chemical Engineering*. 2012;39:41–46.

5 Li Z, Kind M, Gruenewald G. Modeling fluid dynamics and growth kinetics in fluidized bed spray granulation. *The Journal of Computational Multiphase Flows*. 2010;2(4):235–248.

6 Pepiot P, Desjardins O. Numerical analysis of the dynamics of two- and three-dimensional fluidized bed reactors using an Euler–Lagrange approach. *Powder Technology*. 2012;220:104–121.

7 Schellander D, Schneiderbauer S, Pirker S. Numerical study of dilute and dense polydispersed gas–solid two-phase flows using an Eulerian and Lagrangian hybrid model. *Chemical Engineering Science*. 2013;95:107–118.

8 Schneiderbauer S, Aigner A, Pirker S. A comprehensive frictional-kinetic model for gas–particle flows: Analysis of fluidized and moving bed regimes. *Chemical Engineering Science*. 2012;80:279–292.

9 Tsuo YP, Gidaspow D. Computation of flow patterns in circulating fluidized-beds. *AIChE Journal*. 1990;36(6):885–896.

25

0 Wen C, Yu YH. Mechanics of fluidization. In: *The Chemical Engineering Progress Symposium Series*, vol. 62. 1966; pp. 100–111.

1 Agrawal K, Loezos PN, Syamlal M, Sundaresan S. The role of meso-scale structures in rapid gas–solid flows. *Journal of Fluid Mechanics.* 2001;445:151–185.

2 Capecelatro J, Desjardins O, Fox RO. Strongly coupled fluid–particle flows in vertical channels. I. Reynolds-averaged two-phase turbulence statistics. *Physics of Fluids.* 2016;28:033306.

3 Capecelatro J, Desjardins O, Fox RO. Strongly coupled fluid–particle flows in vertical channels. II. Turbulence modeling. *Physics of Fluids.* 2016;28:033307.

4 Chen J, Wang S, Sun D, Lu H, Gidaspow D, Yu H. A second-order moment method applied to gas–solid risers. *AIChE Journal.* 2012;58(12):3653–3675.

5 Dunn DM, Squires KD. Modeling dilute gas–solid flows using a polykinetic moment method approach. *Journal of Fluids Engineering.* 2016;138(4):041303.

6 Dutta A, Constales D, Heynderickx GJ. Applying the direct quadrature method of moments to improve multiphase FCC riser reactor simulation. *Chemical Engineering Science.* 2012; 83:93–109.

7 Hrenya CM, Sinclair JL. Effects of particle–phase turbulence in gas–solid flows. *AIChE Journal.* 1997;43(4):853–869.

8 Lu H, Chen J, Liu G, Lu H, Li D, Zhao F. Simulated second-order moments of clusters and dispersed particles in riser. *Chemical Engineering Science.* 2013;101:800–812.

9 Passalacqua A, Fox RO, Garg R, Subramaniam S. A fully coupled quadrature-based moment method for dilute to moderately dilute fluid–particle flows. *Chemical Engineering Science.* 2010;65(7):2267–2283.

0 Sinclair J, Jackson R. Gas-particle flow in a vertical pipe with particle-particle interactions. *AIChE Journal.* 1989;35(9):1473–1486.

26

1 Fox RO. On multiphase turbulence models for collisional fluid–particle flows. *Journal of Fluid Mechanics*. 2014;742:368–424.

2 Kajishima T, Takiguchi S. Interaction between particle clusters and particle-induced turbulence. *International Journal of Heat and Fluid Flow*. 2002;23:639–646.

3 Capecelatro J, Desjardins O, Fox RO. Numerical study of collisional particle dynamics in cluster-induced turbulence. *Journal of Fluid Mechanics*. 2014;747(R2).

4 Capecelatro J, Desjardins O, Fox RO. Effect of domain size on fluid–particle statistics in homogeneous, gravity-driven, cluster-induced turbulence. *Journal of Fluids Engineering*. 2015;138(4):041301.

5 Capecelatro J, Desjardins O, Fox RO. On fluid–particle dynamics in fully developed cluster-induced turbulence. *Journal of Fluid Mechanics*. 2015;780:578–635.

6 Capecelatro J, Desjardins O. An Euler–Lagrange strategy for simulating particle-laden flows. *Journal of Computational Physics*. 2013;238:1–31.

7 Igci Y, Andrews AT, Sundaresan S, Pannala S, O'Brien T. Filtered two-fluid models for fluidized gas-particle suspensions. *AIChE Journal*. 2008;54(6):1431–1448.

8 Milioli CC, Milioli FE, Holloway W, Agrawal K, Sundaresan S. Filtered two-fluid models of fluidized gas-particle flows: New constitutive relations. *AIChE Journal*. 2013;59(9):3265–3275.

9 Parmentier JF, Simonin O, Delsart O. A functional subgrid drift velocity model for filtered drag prediction in dense fluidized bed. *AIChE Journal*. 2012;58(4):1084–1098.

0 Garzó V, Tenneti S, Subramaniam S, Hrenya CM. Enskog kinetic theory for monodisperse gas–solid flows. *Journal of Fluid Mechanics*. 2012;712:129–168.

1 Jenkins JT, Savage SB. A theory for the rapid flow of identical, smooth, nearly elastic, spherical particles. *Journal of Fluid Mechanics*. 1983;130:187–202.

27

2 Passalacqua A, Fox RO. Advanced continuum modelling of gas–particle flows beyond the hydrodynamic limit. *Applied Mathematical Modelling.* 2011;35(4):1616–1627.

3 Desjardins O, Fox RO, Villedieu P. A quadrature-based moment method for dilute fluid–particle flows. *Journal of Computational Physics.* 2008;227(4):2514–2539.

4 Fox RO. A quadrature-based third-order moment method for dilute gas–particle flows. *Journal of Computational Physics.* 2008;227(12):6313–6350.

5 Chalons C, Fox RO, Massot M. A multi-Gaussian quadrature method of moments for gas–particle flows in a LES framework. In: *Proceedings of the Summer Program.* Center for Turbulence Research, Stanford University. 2010; pp. 347–358.

6 Fox RO. Higher-order quadrature-based moment methods for kinetic equations. *Journal of Computational Physics.* 2009;228(20):7771–7791.

7 Passalacqua A, Fox RO. Simulation of mono- and bidisperse gas–particle flow in a riser with a third-order quadrature-based moment method. *Industrial & Engineering Chemistry Research.* 2012;52(1):187–198.

8 Passalacqua A, Galvin JE, Vedula P, Hrenya CM, Fox RO. A quadrature-based kinetic model for dilute non-isothermal granular flows. *Communications in Computational Physics.* 2011;10(01):216–252.

9 Vié A, Chalons C, Fox RO, Laurent F, Massot M. A multi-Gaussian quadrature method of moments for simulating high Stokes number turbulent two-phase flows. In: *Annual Research Brief.* Center for Turbulence Research, Stanford University. 2012;.

0 Yuan C, Fox RO. Conditional quadrature method of moments for kinetic equations. *Journal of Computational Physics.* 2011;230(22):8216–8246.

1 Vié A, Doisneau F, Massot M. On the anisotropic Gaussian velocity closure for inertial-particle laden flows. *Communications in Computational Physics.* 2015;17(01):1–46.

28

2 Levermore CD, Morokoff WJ. The Gaussian moment closure for gas dynamics. *SIAM Journal on Applied Mathematics.* 1998;59(1):72–96.

3 Syamlal M, Rogers W, O'Brien TJ. MFIX documentation: Theory guide. *National Energy Technology Laboratory, US Department of Energy, Technical Note DOE/METC-95/1013 and NTIS/DE95000031.* 1993;.

4 Gibilaro LG, Gallucci K, Di Felice R, Pagliai P. On the apparent viscosity of a fluidized bed. *Chemical engineering science.* 2007;62(1):294–300.

5 Fox RO, Vedula P. Quadrature-based moment model for moderately dense polydisperse gas–particle flows. *Industrial & Engineering Chemistry Research.* 2009;49(11):5174–5187.

6 Marchisio DL, Fox RO. *Computational models for polydisperse particulate and multiphase systems.* Cambridge, UK: Cambridge University Press. 2013.

7 Lun CKK, Savage SB, Jeffrey DJ, Chepurniy N. Kinetic theories for granular flow: inelastic particles in Couette flow and slightly inelastic particles in a general flowfield. *Journal of Fluid Mechanics.* 1984;140:223–256.

8 Carnahan NF, Starling KE. Equation of state for nonattracting rigid spheres. *The Journal of Chemical Physics.* 1969;51(2):635–636.

9 Ma D, Ahmadi G. A kinetic-model for rapid granular flows of nearly elastic particles including interstitial fluid effects. *Powder Technology.* 1988;56(3):191–207.

0 Bhatnagar PL, Gross EP, Krook M. A model for collision processes in gases. I. Small amplitude processes in charged and neutral one-component systems. *Physical Review.* 1954; 94(3):511.

1 Kopp J. Efficient numerical diagonalization of Hermitian 3×3 matrices. *International Journal of Modern Physics C.* 2008;19(03):523–548.

29

2 Vikas V, Wang ZJ, Passalacqua A, Fox RO. Realizable high-order finite-volume schemes for quadrature-based moment methods. *Journal of Computational Physics.* 2011;230(13):5328–5352.

3 Vikas V, Wang ZJ, Fox RO. Realizable high-order finite-volume schemes for quadrature-based moment methods applied to diffusion population balance equations. *Journal of Computational Physics.* 2013;249:162–179.

4 Kong B, Fox RO. A solution algorithm for fluid–particle flows across all flow regimes. *Journal of Computational Physics.* 2017;(in revision).

5 Passalacqua A, Fox RO. Implementation of an iterative solution procedure for multi-fluid gas–particle flow models on unstructured grids. *Powder Technology.* 2011;213(1):174–187.

6 Yuan C, Kong B, Passalacqua A, Fox RO. An extended quadrature-based mass-velocity moment model for polydisperse bubbly flows. *The Canadian Journal of Chemical Engineering.* 2014;92(12):2053–2066.

30

List of Figures

31

Figure 1: Example of 2-D Gauss–Hermite quadrature ($N_{hq} = 4$, circles), for a velocity distribution (contour lines) with $\boldsymbol{U}_{p,x} = \boldsymbol{U}_{p,y} = 0$ and $\mathbf{P}_{p,xx} = \mathbf{P}_{p,yy} = 1, \mathbf{P}_{p,xy} = 0.5$.

32

(a) $L_x/\mathcal{L} = 8$ (b) $L_x/\mathcal{L} = 32$ (c) $L_x/\mathcal{L} = 129$
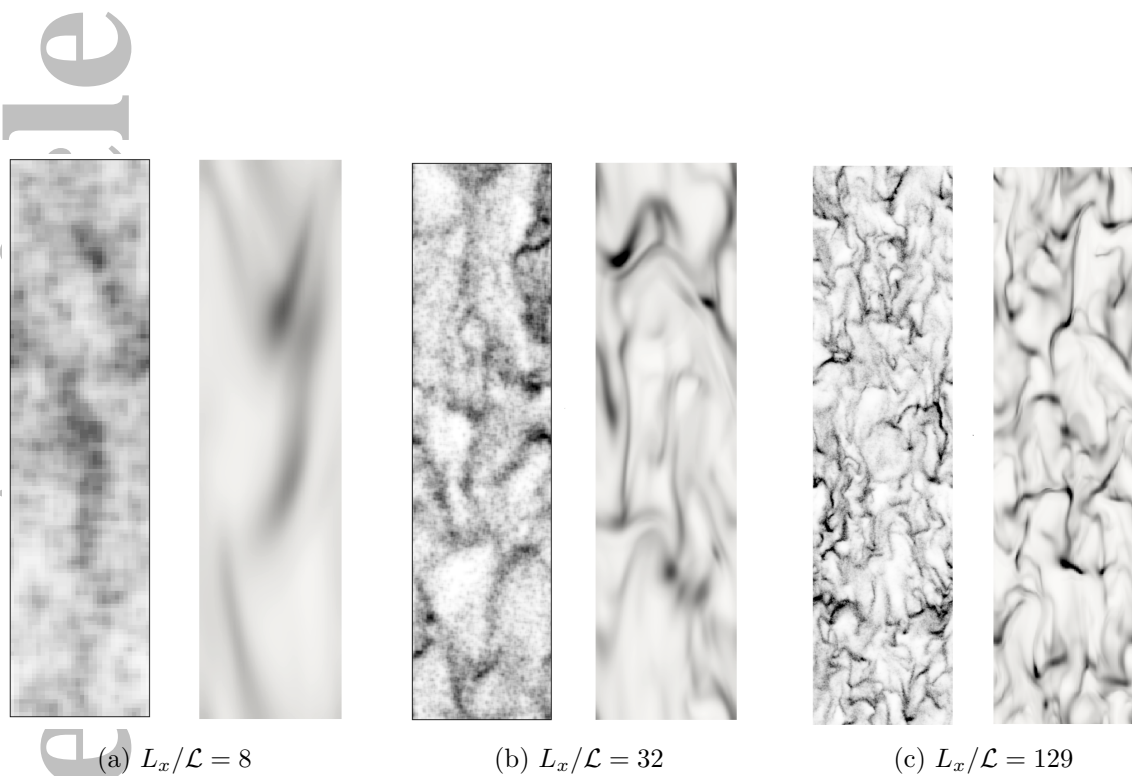
Figure 2: The instantaneous fields for α_p for $L_x/\mathcal{L} = 8, 32$ and 129. The figures on the left are from the EL simulations, and those on the right are from the EE-AG simulations, plotted with a scale of $0 < \alpha_p < 0.05$.

33
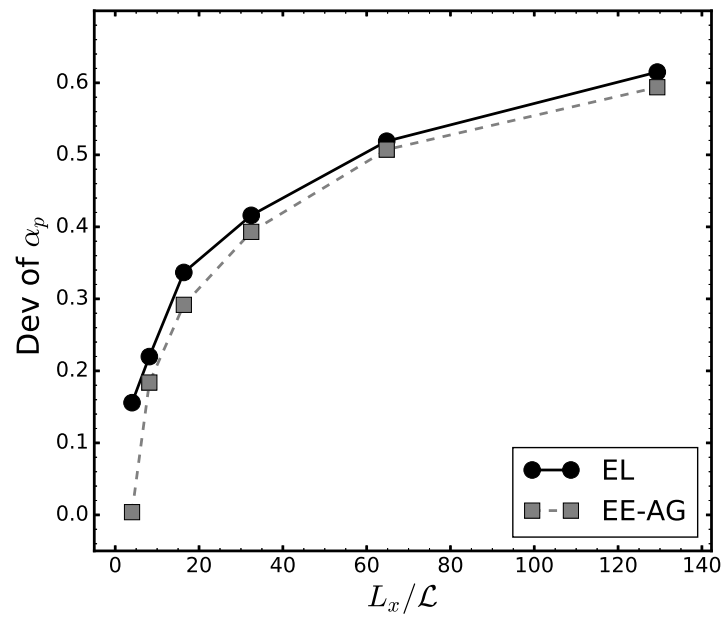
Figure 3: Deviation of volume fraction fluctuations from a corresponding random distribution of particles as a function of domain size.

34

(a) $L_x/\mathcal{L} = 65$ (b) $L_x/\mathcal{L} = 129$
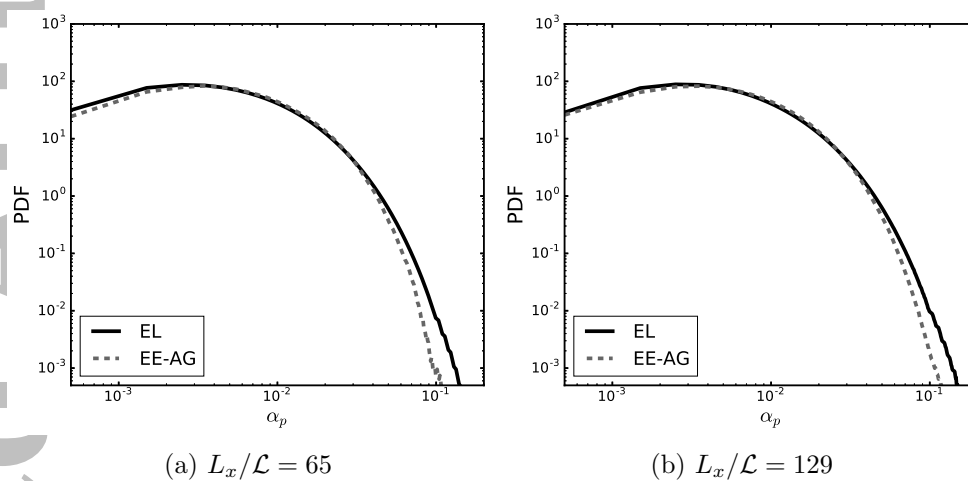
Figure 4: Probability density function (PDF) of particle volume fraction for $L_x/\mathcal{L} = 65$ and 129.
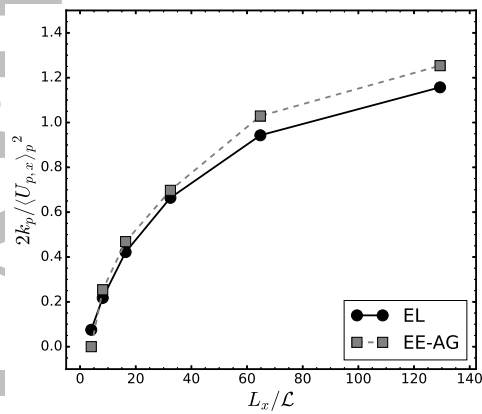
35
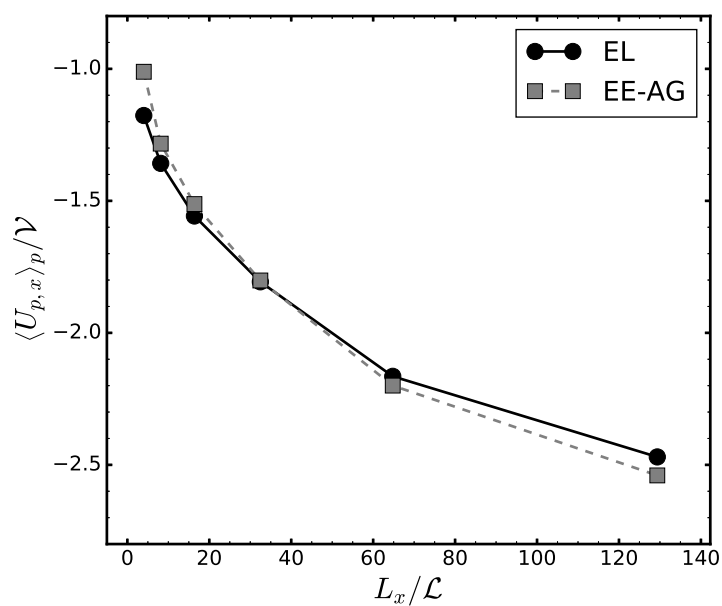
Figure 5: Mean particle settling velocity normalized by the terminal velocity of an isolated particle, $\langle U_{p,x} \rangle_p / \mathcal{V}$, in a corresponding flow as a function of domain size.
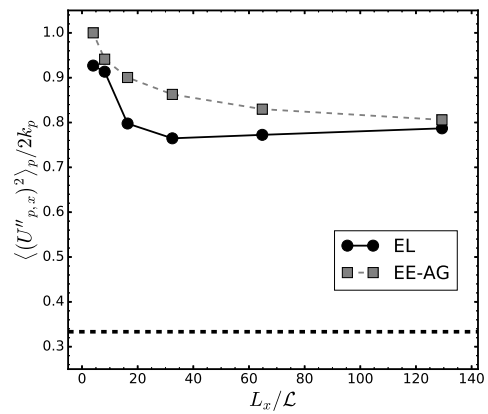
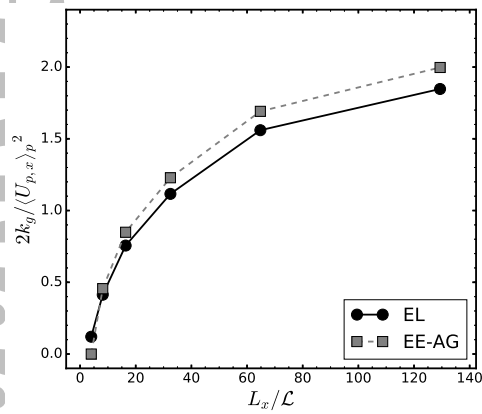36
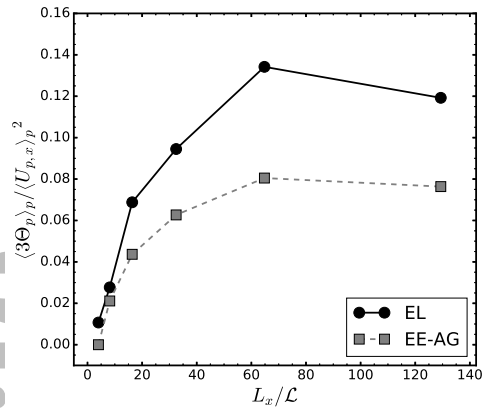
(a) Particle-phase granular energy
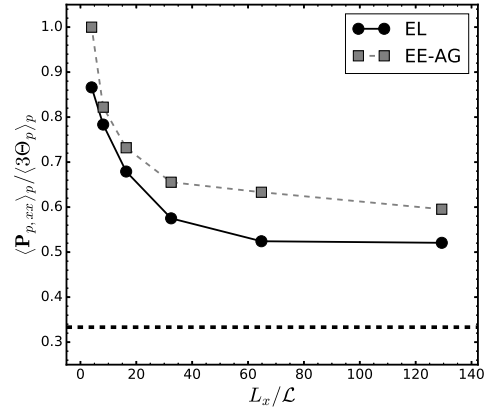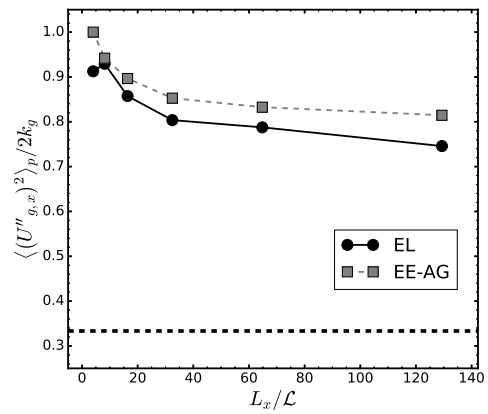
(b) Anisotropy of granular energy

(c) Particle-phase TKE

(d) Anisotropy of particle-phase TKE

(e) Gas-phase TKE

(f) Anisotropy of gas-phase TKE

Figure 6: One-point phasic fluctuating energies and their vertical component contribution. The dashed line in the right column indicates the isotropic value.
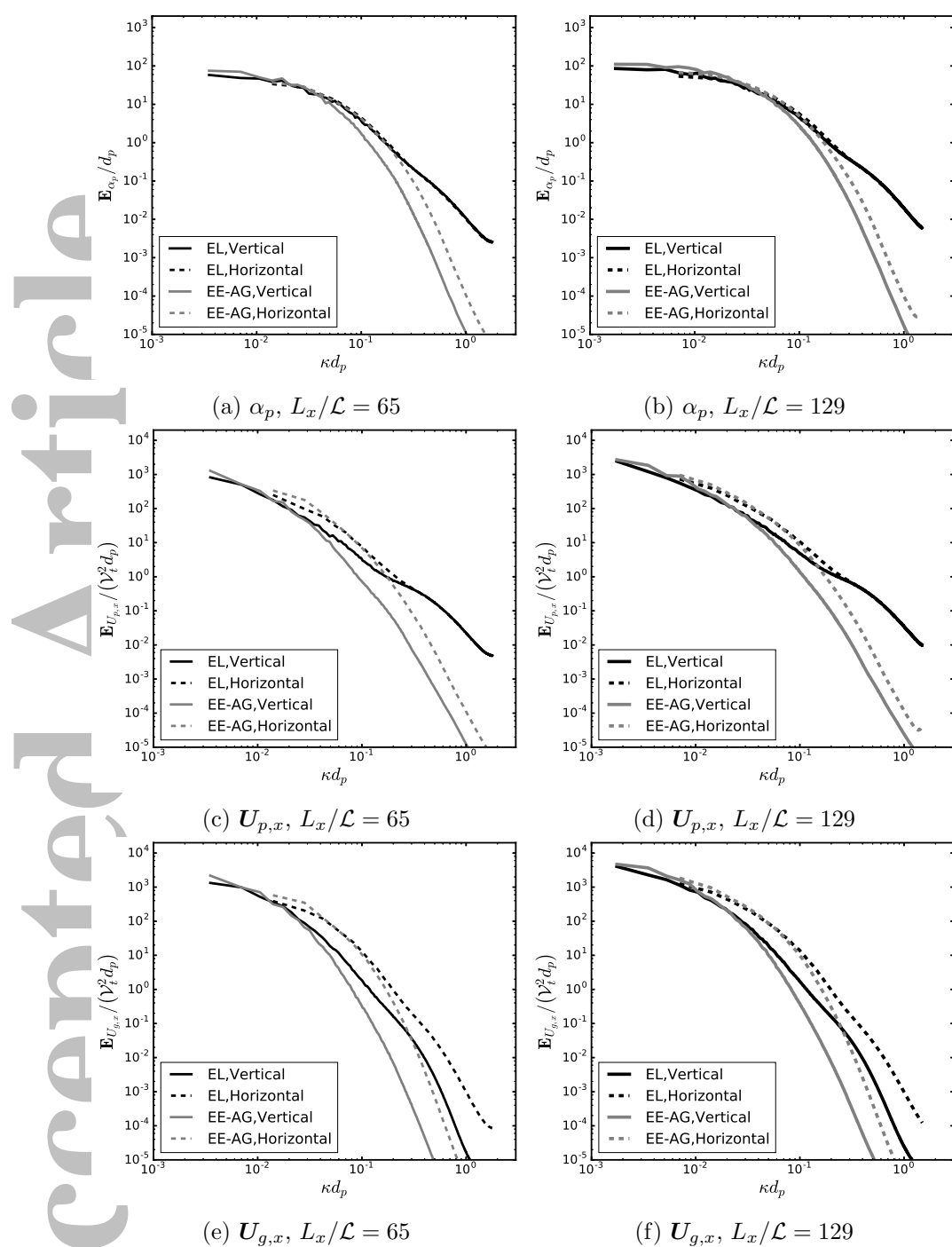
37

(a) α_p, $L_x/\mathcal{L} = 65$

(b) α_p, $L_x/\mathcal{L} = 129$

(c) $\boldsymbol{U}_{p,x}$, $L_x/\mathcal{L} = 65$

(d) $\boldsymbol{U}_{p,x}$, $L_x/\mathcal{L} = 129$

(e) $\boldsymbol{U}_{g,x}$, $L_x/\mathcal{L} = 65$

(f) $\boldsymbol{U}_{g,x}$, $L_x/\mathcal{L} = 129$

Figure 7: Energy spectral density of α_p, $\boldsymbol{U}_{p,x}$ and $\boldsymbol{U}_{g,x}$ for $L_x/\mathcal{L} = 65$ and 129.

38

(a) $L_x/\mathcal{L} = 65$, vertical

(b) $L_x/\mathcal{L} = 129$, vertical

(c) $L_x/\mathcal{L} = 65$, horizontal

(d) $L_x/\mathcal{L} = 129$, horizontal
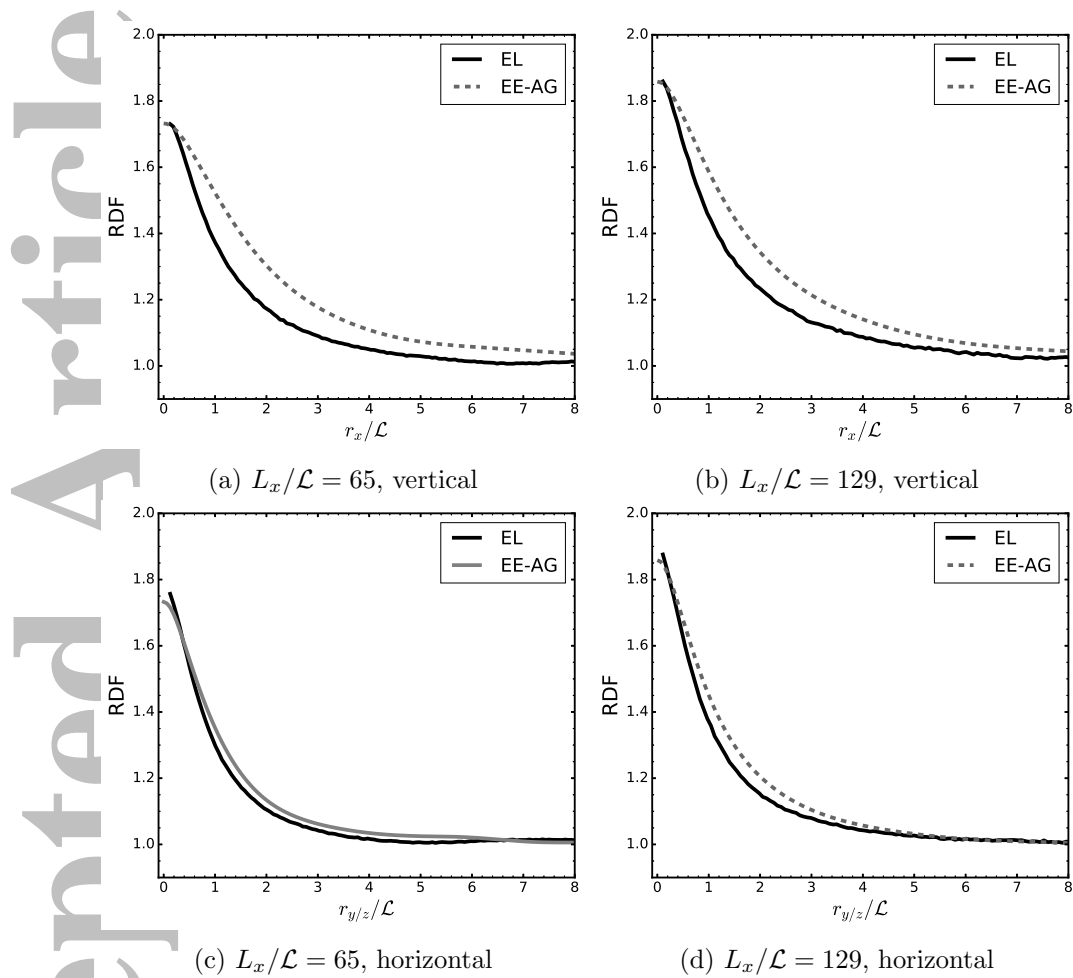
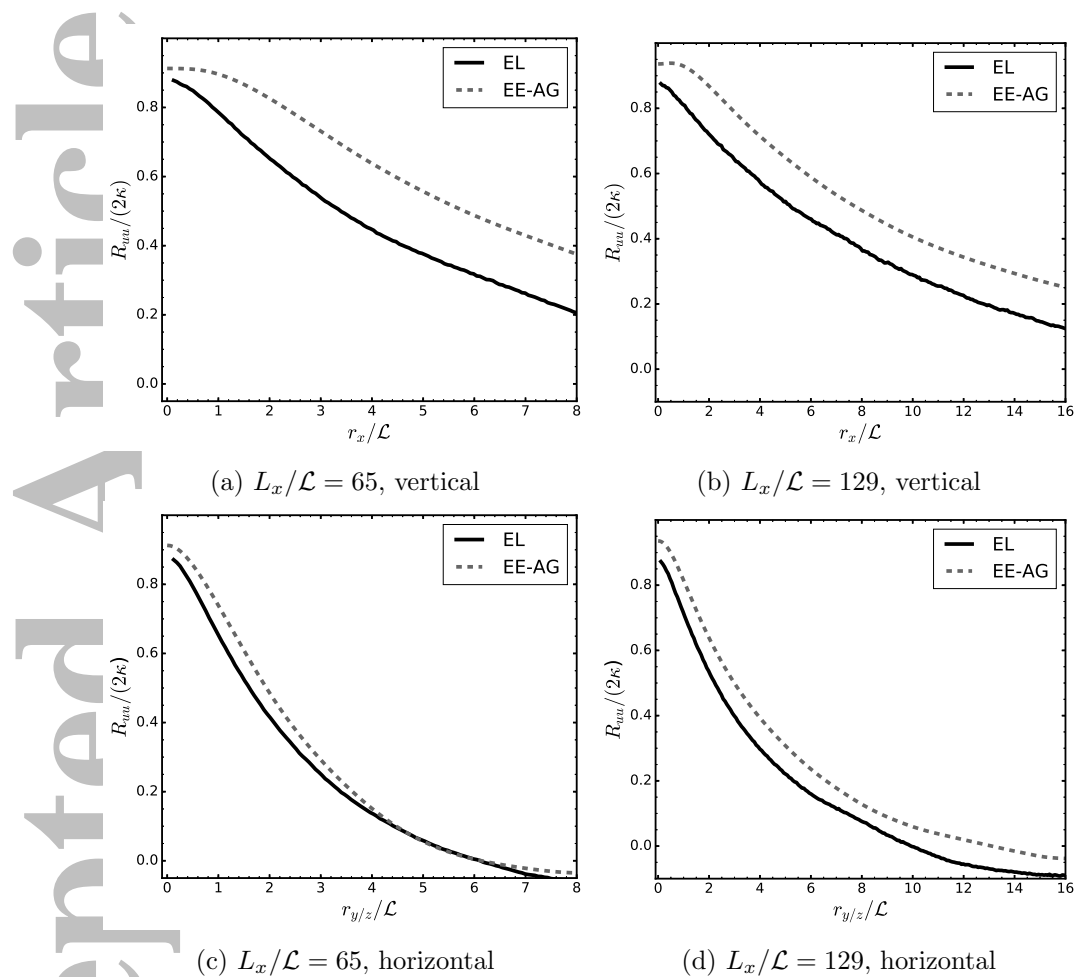Figure 8: Radial distribution function of particle volume fraction for $L_x/\mathcal{L} = 65$ and 129.

39

(a) $L_x/\mathcal{L} = 65$, vertical

(b) $L_x/\mathcal{L} = 129$, vertical

(c) $L_x/\mathcal{L} = 65$, horizontal

(d) $L_x/\mathcal{L} = 129$, horizontal

Figure 9: Two-point spatial cross-correlation function of $\boldsymbol{U}_{p,x}$ for $L_x/\mathcal{L} = 65$ and 129.

40

List of Tables

41

Table 1: Parameters employed in CIT flow simulations.

$\langle \alpha_p \rangle = 0.01$	$\rho_p = 1000$ kg/m^3	$\rho_g = 1$ kg/m^3	$d_p = 90$ μm
$e = 0.9$	$\nu_g = 1.8 \times 10^{-5}$ m^2/s	$\boldsymbol{g} = -4.0004\boldsymbol{e}_x$ m/s^2	CFL $= 0.4$

42